JGR Solid Earth

RESEARCH ARTICLE
10.1029/2022JB025511

Preparatory Slip in Laboratory Faults: Effects of Roughness and Load Point Velocity

Simon Guérin-Marthe[1], Grzegorz Kwiatek[1], Lei Wang[1], Audrey Bonnelye[1,2], Patricia Martínez-Garzón[1], and Georg Dresen[1,3]

[1]Helmholtz Centre Potsdam, GFZ German Research Centre for Geosciences, Section 4.2: Geomechanics and Scientific Drilling, Potsdam, Germany, [2]Free University Berlin, Berlin, Germany, [3]University of Potsdam, Potsdam, Germany

Key Points:

- Acoustic emissions highlight the complex preparatory phase prior stick-slips on rough faults
- Preparatory slip increases with roughness and the duration of the preparatory phase decreases with increasing load point velocity
- Rough and heterogeneous faults are more stable than smooth faults, but can become unstable with a small increase of load point velocity

Supporting Information:

Supporting Information may be found in the online version of this article.

Correspondence to:

S. Guérin-Marthe,
simon-gm@hotmail.fr

Citation:

Guérin-Marthe, S., Kwiatek, G., Wang, L., Bonnelye, A., Martínez-Garzón, P., & Dresen, G. (2023). Preparatory slip in laboratory faults: Effects of roughness and load point velocity. *Journal of Geophysical Research: Solid Earth*, *128*, e2022JB025511. https://doi.org/10.1029/2022JB025511

Received 30 AUG 2022
Accepted 16 MAR 2023

Author Contributions:

Conceptualization: Simon Guérin-Marthe
Formal analysis: Simon Guérin-Marthe, Grzegorz Kwiatek, Georg Dresen
Funding acquisition: Patricia Martínez-Garzón
Investigation: Simon Guérin-Marthe, Lei Wang, Georg Dresen
Methodology: Simon Guérin-Marthe, Lei Wang
Resources: Audrey Bonnelye, Georg Dresen
Software: Grzegorz Kwiatek
Supervision: Audrey Bonnelye, Patricia Martínez-Garzón, Georg Dresen

Abstract Aseismic slip may occur during a long preparatory phase preceding earthquakes, and what controls it remains poorly understood. In this study, we explored the role of load point velocity and surface roughness on slow slip during the preparatory stage prior to stick-slip events. To that end, we conducted displacement-rate controlled friction experiments by imposing varying load point velocities on sawcut granite samples with different surface roughness at a confining pressure of 35 MPa. We measured the average slip along the fault with the recorded far-field displacements and strain changes, while acoustic emission sensors and local strain gages were used to capture local slip variations. We found that the average amount of aseismic slip during the preparatory stage increases with roughness, whereas precursory slip duration decreases with increased load point velocity. These results reveal a complex slip pattern on rough faults which leads to dynamic ruptures at high load point velocities.

Plain Language Summary Earthquakes occur mostly along preexisting faults in the earth crust. These faults exhibit various geometrical complexities and are subjected to different strain rates. In the laboratory, we produce earthquake analogs by sliding sawcut granite blocks. We vary the geometrical complexity of the faults by roughening their surfaces and modify the strain rate by displacing the blocks at varying velocities. Under these different conditions, we measure how the forces accumulated by friction are released, by measuring stresses and displacements applied on the block's edges, using local strain deformation sensors, and by recording very small earthquakes occurring during sliding along the sawcut faults. We find that smooth sawcut faults tend to release all the energy accumulated very abruptly, after a very small amount of slip, regardless of the load point velocity applied. The processes leading to failure in the case of a rough fault are much more complex, involving a large amount of slip, and numerous small earthquakes which are distributed heterogeneously in space and time.

1. Introduction

A preparation phase preceding dynamic ruptures has been observed for a large number of natural earthquakes (Bouchon et al., 2013; Durand et al., 2020; A. Kato et al., 2012; Ruiz et al., 2014). Precursory slip was found to last from several days to several months, and involves the occurrence of foreshocks and/or slip acceleration around the future coseismic slip area (Ruiz et al., 2014). A similar preparatory phase is observed prior to dynamic ruptures in the laboratory (Dresen et al., 2020; Yamashita et al., 2021). It starts at the onset of yielding, when some distributed slip along samples surfaces is detected. Slip is often accompanied by an increase in Acoustic Emission (AE) activity (Goebel et al., 2012; McLaskey & Lockner, 2014). The preparatory phase in laboratory stick-slip experiments lasts a few seconds to tens of seconds (Scholz et al., 1972). The nucleation phase may be included in the preparatory phase and occurs at a shorter time scale prior to instabilities. The nucleation process has been observed in the field, sometimes lasting a few seconds (Tape et al., 2018) and in the laboratory, lasting a few milliseconds (Latour et al., 2013). Nucleation involves the growth of a patch slipping faster than the surrounding fault (Latour et al., 2013; Rice, 1983). The patch is bounded by a rupture front accelerating when it reaches a critical nucleation size L_c, up to velocities controlled by the medium wave speed. The final extent of this patch defines the coseismic slip area. As discussed in McLaskey and Yamashita (2017), in the continuum case where L_c is smaller than the sample size, the instability results from the compliance of the medium, slip eventually accelerates and localizes within a nucleation zone (Ohnaka et al., 1986; Rice, 1993). In cases, a long preparatory phase may occur before a slip event, where the whole surface starts slipping slowly (Yamashita et al., 2022). If L_c is larger than the sample's dimension and slip

Validation: Lei Wang, Audrey Bonnelye, Georg Dresen
Visualization: Simon Guérin-Marthe
Writing – original draft: Simon Guérin-Marthe
Writing – review & editing: Simon Guérin-Marthe, Grzegorz Kwiatek, Lei Wang, Audrey Bonnelye, Patricia Martínez-Garzón, Georg Dresen

affects the entire fault, the sample behaves as a spring-slider block, and if the stiffness of the loading apparatus and the whole sample combined is less than the fault weakening rate, slip becomes unstable (Byerlee, 1970; Ruina, 1983).

Previous studies have revealed that the preparatory and nucleation phase prior to dynamic instability can be explained by some combination of the "cascade" and the "preslip" models (Ellsworth & Beroza, 1995; McLaskey, 2019). Once a fault is close to failure, observations suggest that loading of asperities due to aseismic preslip and by stress transfer between foreshocks may occur concurrently (Kato & Ben-Zion, 2021; McLaskey, 2019; Yamashita et al., 2021). However, how preparatory and nucleation phases are linked and what controls the spatio-temporal distribution of slip during run-up to failure is still poorly understood. In addition, it remains unclear in which cases rapid stick-slip instabilities develop, and which of the continuum or spring-slider model better represents the samples behavior.

Several factors have been proposed to influence the preparatory phase and the failure mode of a fault, including roughness (Harbord et al., 2017; Morad et al., 2022; Ohnaka & Shen, 1999; Okubo & Dieterich, 1984), load point velocity (Guérin-Marthe et al., 2019; Kato et al., 1992; Marone, 1998; McLaskey & Yamashita, 2017), injection rate for permeable faults (Wang et al., 2020), (effective) normal stress state (Latour et al., 2013; Passelègue et al., 2020) and healing time (Marone, 1998). Looking at these different parameters individually reveals a complex picture. Morad et al. (2022) argued that an optimal roughness for triggering stick-slip instabilities on sawcut faults may exist, and Harbord et al. (2017) suggested that fault stability in granite is governed by a combination of roughness and normal stress almost irrespective of velocity strengthening and weakening behavior. Earlier work from Ohnaka (1973) already showed that for a given roughness, slip stability depends on the hardness of the two fault blocks in contact. Zhuo et al. (2022) highlighted controversial findings concerning the effect of load point velocity on slip. In cases, enhanced load point velocities were observed to promote instabilities (Guérin-Marthe et al., 2019; Kato et al., 1992; McLaskey & Yamashita, 2017), while other studies suggested the opposite (Karner & Marone, 2000; Ohnaka, 1973). However, cumulative slip (Zhuo et al., 2022), healing times and hold periods in slide-hold-slide tests (Guerin-Marthe, 2019) varied between these studies possibly affecting slip.

In this study, we explore the effect of load point velocity and surface roughness on precursory slip during the preparatory stage prior to stick-slip events under upper crustal pressure conditions (corresponding to about 1 km depth). Although the load point velocity and roughness effects on fault stability have both been investigated separately, this work aims at complementing previous studies in several ways. First, the load point velocity is studied under triaxial stress conditions at elevated confining pressure representative of the upper crust (35 MPa) on granite samples. In addition, the effect of load point velocity is compared for samples with different fault roughness. Comparable experimental conditions and increased load point velocity were already observed to be required for triggering stick-slips (McLaskey & Lockner, 2014). Here, we extend these results by quantitatively comparing experiments performed at different load point velocities and at different roughness conditions. In particular, we focus on the spatio-temporal distribution of slip prior and during instabilities using far-field mechanical data, local strain gage sensors and a dense network of piezoelectric transducers which enable us to track AEs occurring during slip episodes along the fault. This set of experiments aims at reconciling the spring-slider and continuum views of slip instability. We discuss the combined effects of roughness and load point velocity, and show how failure mode and the different slip stages may be controlled by a combination of loading system stiffness and nucleation length to sample and asperity size ratio (McLaskey & Yamashita, 2017).

2. Materials and Methods

2.1. Granite Samples and Surface Preparation

Three cylindrical samples were prepared from La Peyratte granite with dimensions of 100 mm in length and 50 mm in diameter (Young's modulus $E \approx 75$ GPa and Poisson's ratio $\nu \approx 0.25$, see Figure S3 in Supporting Information S1). The grain size of the granite samples ranges from 0.5 to 1.5 mm (David et al., 1999). The samples were precut at an angle $\theta = 30°$ to the sample axis. All sawcut surfaces were precision-ground and polished using a powder composed of silicon carbide particles with a diameter of 9 µm. We prepared one rough fault surface (sample R1) by sandblasting it with silicon carbide particles producing a root mean square asperity height of Z_{rms} = 12–16 µm and some long wavelength relief. In contrast, the smooth surfaces (samples S1 and S2) are characterized by $Z_{rms} \approx 3$ µm (Figure S3 in Supporting Information S1).

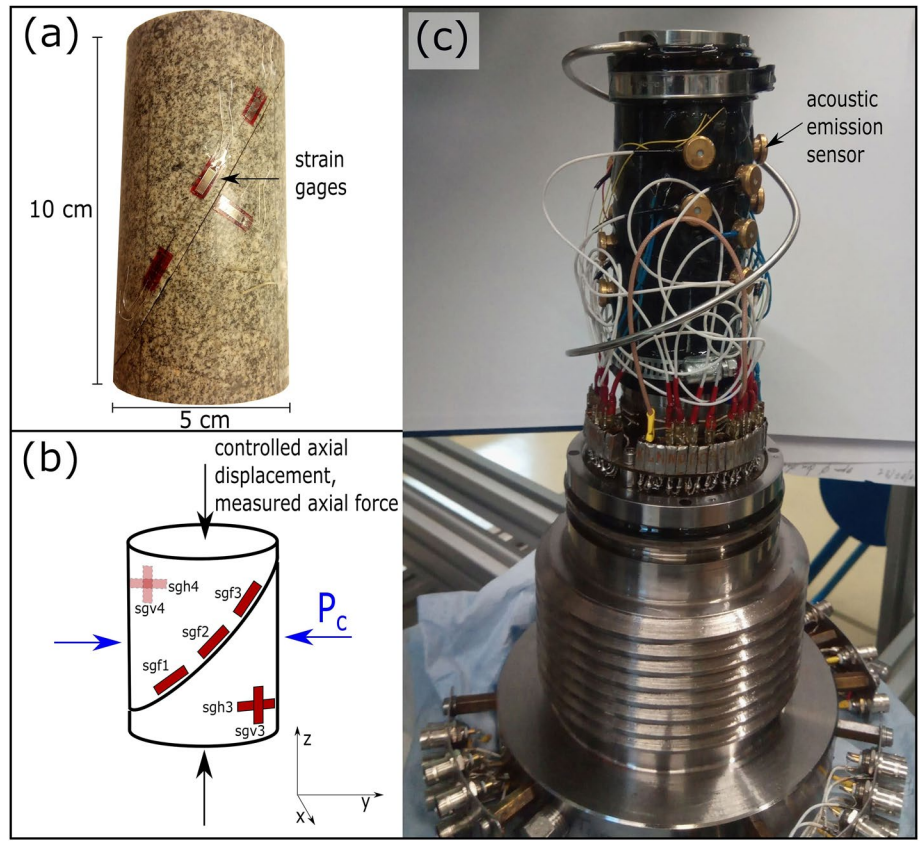

Figure 1. (a) Sawcut granite blocks with strain gages glued directly on the sample. (b) Schematic view of the strain gages configuration and of the loading forces. (c) Specimen assembly with the AE sensors placed in brass housings mounted directly on the sample through holes in the rubber jacket.

2.2. Strain Gage Sensors

The samples were all oven-dried for at least 48 hr before mounting strain gages. Specifically, two pairs of orthogonal strain gages attached to the center of two blocks (Figures 1a and 1b) were used to measure the elastic deformation of the rock matrix. Three additional strain gages (sgf1, sgf2, and sgf3) were positioned parallel to the sawcut fault, and centered 4 mm (±1 mm) away from it. The distance between the center of two fault parallel strain gages is about 25 mm (Figure S1 in Supporting Information S1). The strain gages were used to monitor local slip variations along the fault plane. After gluing strain gages, the samples were placed in a rubber jacket, used to isolate them from the oil confining medium.

2.3. Acoustic Emissions Recordings

An array of 16 piezoelectric transducers (1 MHz resonant frequency) surrounding the samples was used to monitor AEs. The sensors were placed in brass housings, which were glued directly on the rock surface using epoxy, through holes pierced in the rubber jacket (Figure 1c). Full AE waveforms, as well as active ultrasonic transmission (UT) measurements were recorded at a sampling rate of 10 MHz with 16-bit amplitude resolution using the 16-channels DAXBox (Prökel) recording system. UT measurements were performed every 10 s throughout the whole experiment and used to calculate and update a time-dependent quasi-anisotropic *P*-wave velocity model composed of five layers perpendicular to and one vertical layer parallel to the loading axis (see e.g., Kwiatek, Charalampidou et al., 2014; Stanchits et al., 2011). *P*-wave arrival times of AEs were automatically picked using the convolutional neural network-type picker based on Ross et al. (2018) trained on past AE experiments. To locate AEs, the Equivalent Differential Time method (e.g., Font et al., 2004) was used and solved using a combination of grid search followed by simplex (e.g., Nelder & Mead, 1965) optimization algorithms while using the time-dependent velocity model derived earlier from UT data. The average AE hypocenter location accuracy is ±2 mm (Stanchits et al., 2011) allowing to monitor local heterogenous deformation.

After hypocenter determination, the relative AE magnitude was estimated as:

$$M_{\mathrm{AE}} = log_{10}\sqrt{\frac{1}{n}\sum_{i=1}^{n}(A_i R_i)^2}, \tag{1}$$

where A_i and R_i are the first P-wave amplitude and source-receiver distance for each individual AE sensor i, respectively (e.g., Dresen et al., 2020; Zang et al., 1998). Magnitude M_{AE} is a relative measure and not directly calibrated to the physical size of the events (see e.g., Dresen et al., 2020 for additional discussion). Finally, a polarity coefficient was calculated for each AE event following Zang et al. (1998):

$$p_{\mathrm{AE}} = \frac{1}{n}\sum_{i=1}^{n} sgn(A_i), \tag{2}$$

using average polarity of first P-wave amplitudes (cf. Figure 3c). This parameter signifies whether the source types of AE events reflect compaction ($0.25 < p_{\mathrm{AE}} \leq 1$), tensile opening ($-1 \leq p_{\mathrm{AE}} < -0.25$) or shearing ($-0.25 \leq p_{\mathrm{AE}} \leq 0.25$) source types (see Zang et al., 1998 for details).

Using the catalog of located AE events above the AE magnitude of completeness of $M^c_{\mathrm{AE}} = 1.8$ (assessed by visual inspection of the magnitude-frequency distribution) we calculated the magnitude-frequency Gutenberg Richter b-value in a moving time window of 200 s (Figure 3b). For each window, the b-value was estimated using the maximum likelihood approach:

$$b = \frac{1}{\overline{M_{\mathrm{AE}}} - M^C_{\mathrm{AE}}}\log_{10}(e), \tag{3}$$

where $\overline{M_{\mathrm{AE}}}$ is the average magnitude of AEs that occurred within each 200-s window and that are above the magnitude of completeness. The estimates were corrected for the bin size (e.g., Guo & Ogata, 1997). The uncertainties of the b-value were estimated following Shi and Bolt (1982), suitable for weakly non-stationary catalogs. Note that the b-value calculated using the relative AE magnitude is not directly comparable to the b-value calculated for natural earthquakes using moment magnitude.

2.4. Triaxial Loading Configuration, Shear Stress and Slip Calculation

The prepared samples were placed in a pressure vessel (Figure 1c) and first loaded hydrostatically up to 35 MPa. The confining pressure was then maintained constant at 35 MPa in all experiments. Samples were deformed at dry conditions using a servo-controlled hydraulic Machine Testing System (MTS 4600). Axial loading was achieved by applying vertical piston displacement rates ranging from 0.05 to 1 μm/s. A linear variable displacement transducer (LVDT) measured Δl_{LVDT}, the total displacement of the machine (with a stiffness of $K_{\mathrm{MTS}} = 0.65 \times 10^9$ N/m or 330 MPa/mm for 5 cm diameter samples) and the specimen (stiffness of 750 MPa/mm). The differential stress ($\sigma_1 - \sigma_3$) was measured using an internal load cell with a precision of ±0.05 MPa.

Mechanical data including differential stress, axial shortening and local strains were recorded continuously at a sampling rate of 10 Hz during the experiments. To better resolve short slip episodes, a high-speed data logging system triggered by the user also recorded with sampling rates between 2 kHz (sample S1) and 5 kHz (samples S2 and R1), during short periods of interest.

In triaxial loading configuration, the average shear stress τ resolved along the inclined sawcut fault plane (angle θ to the cylinder axis) was calculated from the differential stress as:

$$\tau = (\sigma_1 - \sigma_3) \times \sin\theta \times \cos\theta \tag{4}$$

and the average slip s along the fault using:

$$s = \frac{(\Delta l_{\mathrm{LVDT}} - \Delta l_{\mathrm{MTS}} - \Delta l_{\mathrm{RM}})}{\cos\theta} \tag{5}$$

where Δl_{LVDT} is the total axial displacement, Δl_{MTS} is the axial shortening of the loading machine, estimated by Δl_{MTS} = change of the axial force $/K_{\mathrm{MTS}}$, and Δl_{RM} is the axial deformation of rock matrix, as given by

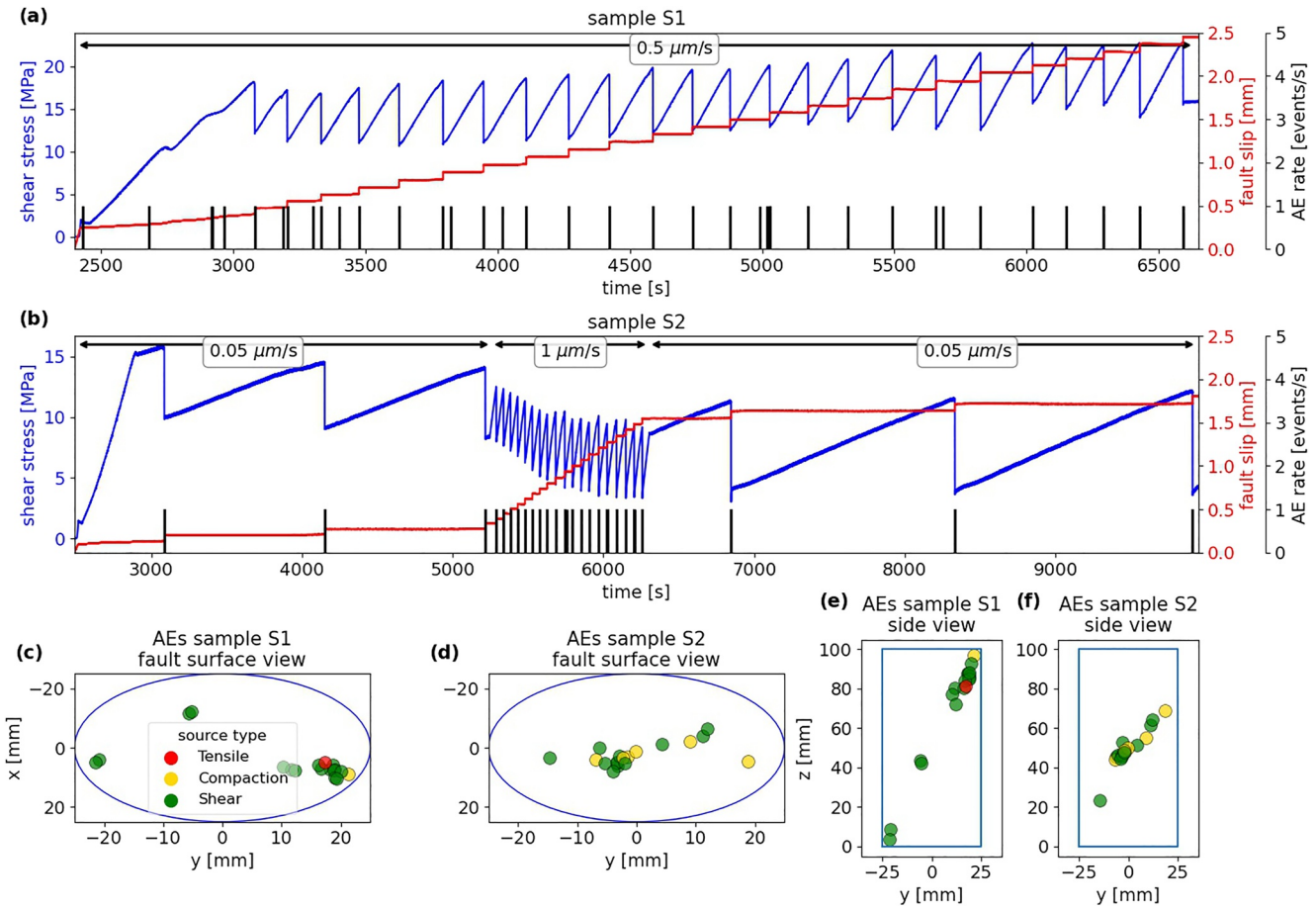

Figure 2. Evolution of shear stress, fault slip and AE rate on smooth faults (a) loaded at a constant displacement rate of 0.5 μm/s using sample S1, (b) at displacement rates of 0.05 and 1 μm/s using sample S2. AE locations and source types for (c) sample S1 fault surface view, (d) sample S2 fault surface view, (e) sample S1 side view, (f) sample S2 side view. The AE source types are classified into tensile, compaction and shear sources based on P-wave first motion polarities (see Equation 2).

$\Delta l_{RM} = (\varepsilon_{sgv3} + \varepsilon_{sgv4})/2 \times L$, where sgv3 and sgv4 are vertical strain gages attached to rock matrix, and $L = 100$ mm is the sample length. Note that the stresses are also corrected for the reduction in nominal contact area between the two parts of the fault during slip. More details about data processing are given in Wang et al. (2020).

3. Results

3.1. Mechanical Response and AE Activity

3.1.1. Smooth Faults

The two samples with smooth sawcut faults were deformed at a constant displacement rate of 0.5 μm/s and at displacement rates alternating between 0.05 μm/s and 1.0 μm/s, respectively (Figures 2a and 2b). Both tests resulted in episodic stick-slip events with recurrence intervals decreasing from about 1,200 s to 60 s with load point velocities v_{lp} increasing by a factor of 20. With progressive slip, sample S1 showed a small increase in peak stress for the stick-slip events, possibly due to progressive gouge formation. The stress drop magnitude associated with the stick-slip events increased with cumulative fault slip, and ranged from 5 MPa for the smallest event of sample S2 at 1 μm/s (see Figure 2b), to 9 MPa for the largest stick-slip event on sample S1, loaded at 0.5 μm/s (see Figure 2a). In contrast, for sample S2 increasing v_{lp} from 0.05 to 1.0 μm/s showed a reduction in peak stress from 15 MPa to about 10 MPa. This was accompanied by a decrease of stress drop magnitude from 7 to 5 MPa (Figure 2b).

In general, preparatory slip on smooth faults is small, between 3 and 10 μm and failure occurs abruptly (i.e., the main slip episode lasts about 2 ms, see Figure 8a). Additionally, we did not resolve any time delay between the

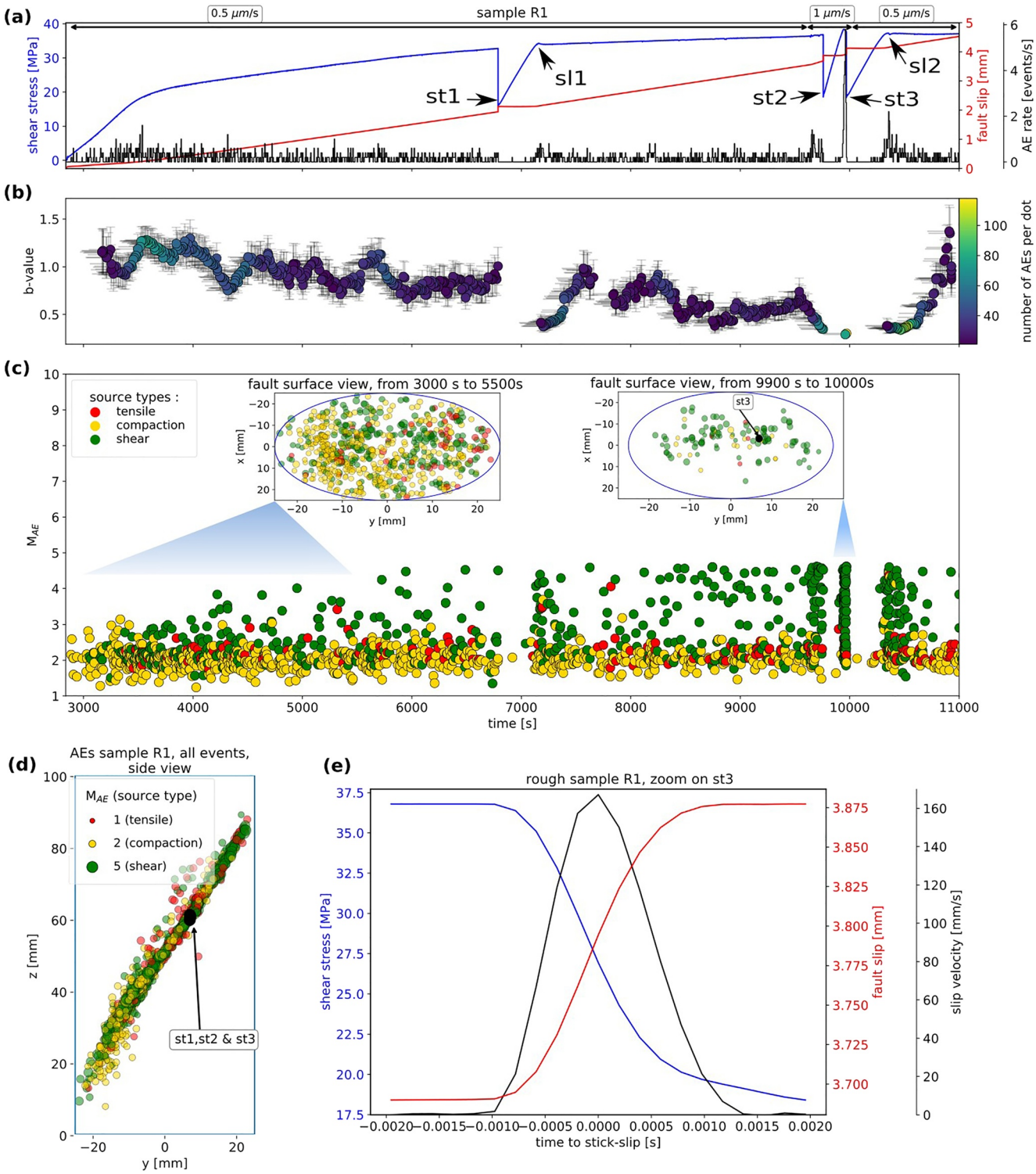

Figure 3. (a) Evolution of shear stress, fault slip and acoustic emission rate on a rough fault under load point velocities of 0.5 and 1 μm/s using sample R1. (b) Time evolution of b-value from AEs recorded on sample R1. The time windows for b-value calculations are indicated by horizontal gray lines, and the number of events during a time window is indicated on the color scale. Uncertainties are reported as vertical gray lines. (c) Time evolution of AE magnitude and AE source types, and fault surface views of corresponding AE hypocenter locations and types at the start of the experiment, and just before stick-slip st3. (d) Side view of all located AEs during the experiment. The black dots indicate the location of the AEs associated with the main stick-slip events. Note that the size of each dot is positively correlated with the amplitude of an AE event. The source types of AE hypocenter are classified into tensile, compaction and shear focal mechanism based on P-wave first motion polarities (see Equation 2). (e) Evolution of shear stress, slip and slip velocity during stick-slip event st3 on the rough fault R1.

different strain gage signals sampled at frequencies up to 5 kHz. Considering the spacing of 2.5 cm between the strain gages (Figure S1 in Supporting Information S1), and assuming a rupture front propagating in the fault plane along the fault dip direction (see Figure 1b), this would result in rupture velocities V_r larger than 125 m/s. During the elastic loading of the locked smooth faults, we observed very little AE activity. However, every single stick-slip event was accompanied by a very large AE, and by an audible sound. Large AE events occurred close to or at the time of the main stress drop ±100 ms, within the accuracy of the synchronized data acquisition systems. These AEs have large and typically clipped waveforms that last several milliseconds. The AE hypocenters of these large events were located on the sawcut faults partly forming localized clusters (Figures 2c–2f). Based on P-wave first motion polarities (Zang et al., 1998), the AEs display predominantly double-couple mechanisms.

3.1.2. Rough Fault

Loading of the samples containing a rough fault resulted in significantly different deformation compared to smooth faults. Beyond a yield stress, the sample assembly shortened by continuous sliding along the fault. At a piston displacement rate of 0.5 μm/s the samples showed stable sliding for about 1.5 mm and hardening with shear stress increasing by about 10 MPa. Sliding was accompanied by prominent AE activity reaching a total of 1,595 events before a sudden stick-slip event (st1) occurred (Figure 3a). AE hypocenters were aligned with the fault and distributed across the entire fault surface (Figure 3d). Initially, during stable slip AEs were dominated by small-magnitude compaction events (Figure 3c), progressively replaced by larger shear events and few tensile source types. A similar shift in AE source types was also observed in stick slip events occurring at confining pressure >100 MPa (Kwiatek, Goebel, et al., 2014). For the rough fault in sample R1, the first stick-slip event (st1) occurred after about 2 mm of stable sliding, with a stress drop of about 16 MPa, terminating the first phase of the test. We note that the AE activity did not increase significantly prior to failure.

After event st1 the fault was locked again and elastic loading resumed to a yield point at a shear stress of about 32 MPa (sl1), which is roughly similar to the peak stress reached before stick-slip event st1 occurred. Stable fault slip initiated at a peak shear stress of 34 MPa and the fault strengthened again but at a smaller rate. This stable sliding episode lasted until the displacement rate v_{lp} was increased to 1 μm/s. Shortly after the displacement rate was increased, two stick-slips occurred (st2 and st3) with stress drops of about 15–20 MPa. Both stick-slip events were preceded by bursts in AE activity.

After the stick-slip event st3, the displacement rate v_{lp} was reset to 0.5 μm/s. The sawcut was locked and loading reached a peak stress of 38 MPa at which a small slow slip event (sl2) initiated a third stable sliding phase. Note that slow slip sl2 is preceded by a burst of AEs similar to the one preceding stick-slip event st2, showing that bursts in AEs are not necessarily followed by rapid stick-slip events.

Sample R2 similarly showed dominantly stable sliding at a piston displacement rate of 0.5 μm/s interrupted by a single very slow slip event. Increasing the load point velocity to 1 μm/s produced oscillatory slips with very small stress drops. For this sample we observed significant wear and gouge production (see Figure S8 in Supporting Information S1).

Overall, AE hypocenters align well with the fault plane in sample R1 (Figure 3d). AE hypocenters from a time window of 100 s just before stick-slip events are widely distributed, but concentrate on local high elevation areas (Figures 3c and 4). In general, the AE events occurring shortly before stick-slip events and slow slip events display larger amplitudes with dominantly shear focal mechanisms (a few compaction events remain smaller in comparison).

The magnitude-frequency distribution of AEs shows a continuous trend of decreasing *b*-value toward the final stick slip event st3 (Figure 3b). This trend is punctuated by short episodes of *b*-value decrease likely associated with local slip events (cf. Dresen et al., 2020).

3.2. Preparatory Slip

3.2.1. Smooth Faults

Here we focus on the preparatory aseismic slip prior to stick-slips on smooth sawcut faults at different load point velocities showing a few representative stick-slip events in greater detail (Figures 5a–5c). Macroscopic slip (see Equation 5) corresponds to the average displacement between the two fault blocks. After stick-slip events, the

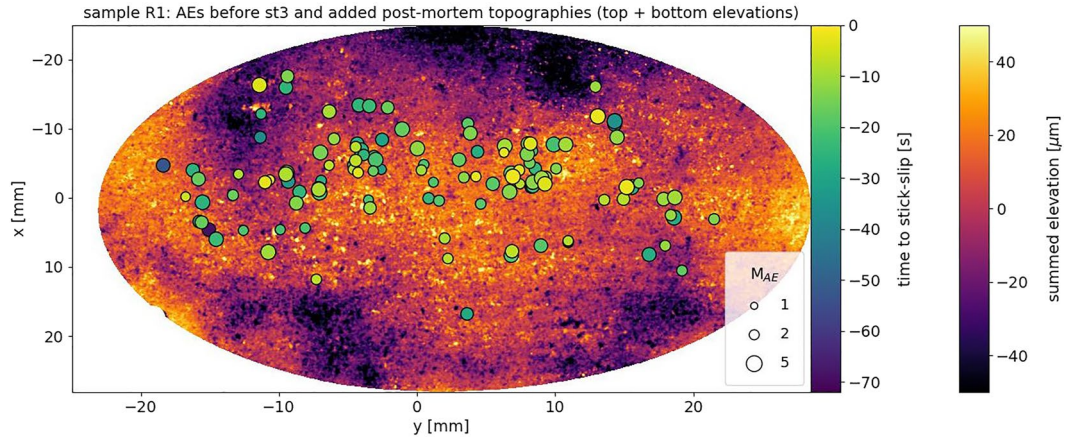

Figure 4. Added topography of the post-mortem rough fault surfaces from sample R1 (top block topography + bottom block topography) with superimposed acoustic emissions before stick-slip event st3.

smooth faults were locked, and no slip between the blocks was observed. Continued loading resulted in elastic deformation of the bulk with linear stress increase with time (e.g., Figures 5a, 4500–5000s). At a yield point, relative slip between the blocks initiated, eventually leading to failure. The total amount of fault slip for the smooth faults ($Z_{rms} \approx 3$ µm) during this preparatory phase is estimated to be about 3–10 µm. The duration of the preparatory phase decreased with increasing load point velocity, from about 200 s at 0.05 µm/s, to 40 s at 0.5 µm/s, and 20 s at 1 µm/s (Figures 5a–5c).

Within 10 s before failure (Figures S6a–S6c in Supporting Information S1), we observed diverging signals from the fault parallel strain gage starting a few seconds before the stick-slips. At $v_{lp} = 0.5$ µm/s, the shear stress started dropping roughly one second before the slip event. At $v_{lp} = 1$ µm/s shear stress decreased approximately 0.5 s before failure. At a low load point velocity of 0.05 µm/s, this weakening phase is hardly observable due to the noise superimposed on stress, slip and deformation signals (Figure S6a in Supporting Information S1).

3.2.2. Rough Faults

Compared to the smooth faults, preparatory slip before slow and fast slip events on the rough fault ($Z_{rms} \approx 14$ µm) showed a more complex behavior (Figures 5d–5f). For example, stick-slip events st1 and st2 occurred without visible slip acceleration (Figure 3a), irrespective of doubling the load point velocity between events (Figures S6d–S6f in Supporting Information S1). This is in contrast to stick-slip st3 and slow slip sl1 and sl2 (Figures 5d–5f). The preparatory phase lasting approximately 200 s corresponds to an amount of slip up to roughly 50 µm (5 times the slip observed on the smooth fault at the same load point velocity) for the two slow slip events sl1, sl2. Prior to stick-slip st3 at $v_{lp} = 1$ µm/s, preparatory slip duration was reduced to 100 s, while the slip amount remained about 50 µm (st3, Figure 5f). Note that preparatory slip started with local slip detected on fault parallel gage sgf1 (Figures 5d–5f and Figure 6), while strain gage sgf2 remained in compression.

Prior to stick-slip st2 (Figure S6e in Supporting Information S1), we did not observe accelerating preparatory slip, instead the fault was creeping continuously. However, after increasing v_{lp} from 0.5 to 1 µm/s (Figure S6e in Supporting Information S1 and Figure 6, around 9,640 s), shear stress fluctuated and AE activity increased during about 100s before the main stick-slip st2. Prior to events st1 (Figure S6d in Supporting Information S1) and st2 (Figure S6f in Supporting Information S1) the fault was creeping at v_{lp} without any observable changes before failure occurred.

3.2.3. Scaling of the Preparatory Slip With Load Point Velocity and Roughness

At constant confining pressure, preparatory slip depends on roughness and the duration of the preparatory slip phase depends on both roughness and load point velocity. To compare the data from the different tests we plot the non-dimensional parameters p1 = $slip/Z_{rms}$ and p2 = (*time-to-event* × *load-point-velocity*)/Z_{rms} (Figure 7c). The normalized slip curves converge but still show distinct differences approaching failure. With onset of fault slip smooth faults remain partially locked with slip rates $<v_{lp.}$ In contrast, in some cases rough faults show accelerating slip toward failure. The slip on the smooth faults increases at a low rate accounting for only a

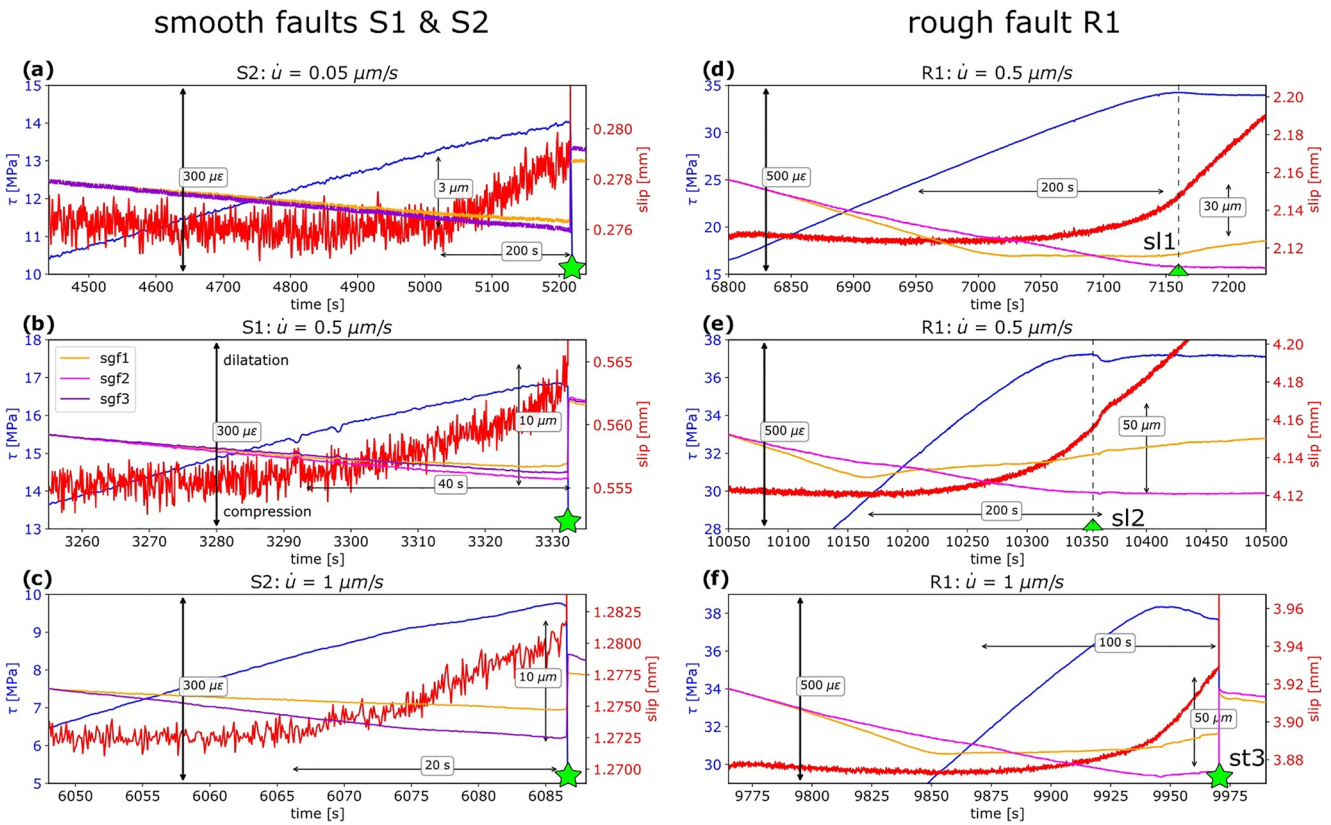

Figure 5. Evolution of shear stress (blue curve), slip (red curve) and fault parallel strain gage signals (purple, pink and yellow curves), during selected phases of the rock deformation experiments. (a–c) Stick-slip events for smooth faults S1 and S2 at load point velocities of (a) v_{lp} = 0.05 μm/s, (b) v_{lp} = 0.5 μm/s and (c) v_{lp} = 1 μm/s. (d, e) Slow-slip events sl1 (d) and sl2 (e) at a load point velocity of v_{lp} = 0.5 μm/s on the rough fault. (f) Stick-slip st3 on the rough fault R1, loaded at v_{lp} = 1 μm/s. The strain signals are offset to zero at the start of the plots, upwards corresponds to dilatation while downwards corresponds to compression. The strain amplitude in με is indicated on each plot. Stick-slip onsets are indicated by green stars, and slow slip onsets, corresponding to the start of shear stress decrease, are indicated by green triangles.

fraction (10%–30%) of the load point velocity (0.1–0.3 v_{lp}, see Figure 7a). On the same rough fault, prior to stick-slip event st3 at v_{lp} = 1 μm/s, slip also accelerated and slightly exceeded the load point velocity v_{lp} before failure (see Figure 7b). These observations indicate that smooth faults may develop a larger slip deficit prior to failure.

3.3. Slip Velocity and Associated Stress Drop During Stick-Slip Events

For all stick-slip events we measured the average slip and stress drop magnitudes using the recordings of axial force, displacement and of three strain gages located at the edges of the sample's sawcut surfaces (see Section 2). Slip velocities were determined for the dynamic slip phase lasting about 2 ms for all tests, using available high-speed data (Figure 8a). At v_{lp} = 1 μm/s, the smooth fault S2 slipped with velocities between 45 and 55 mm/s, the stress drop was around 4.5–6 MPa and the total slip about 60 μm (Figure 8b). For comparison, the preparatory slip velocity on smooth faults ranged from 0.005 μm/s to 0.45 μm/s, at load point velocities of 0.05 μm/s and 1 μm/s, respectively. The total preparatory slip was about 10 μm, which was about 15%–20% of the displacement measured during stick-slip events. On the rough fault the slip velocity reached 160 μm/s at v_{lp} = 1 μm/s, with a stress drop of 18–19 MPa, and total slip of about 200 μm (4 times the amount of preparatory slip). In these experiments, the measured maximum slip velocity increased with decreasing load point velocity, with values larger than 70 mm/s at 0.05 μm/s. Slip velocity was also strongly correlated with stress drop (Figure 8c). However, due to the lower sampling rate of 2 kHz for sample S1, slip velocities for the slip events at 0.5 μm/s were possibly underestimated. When plotting shear stress versus slip (Figure 8b), we obtained an average fault stiffness of $K_{fault} \approx 90$ MPa/mm ($K_{fault} \approx 85$ MPa/mm for the smooth faults, and $K_{fault} \approx 95$ MPa/mm for the rough fault). To estimate fault stiffness K_{fault}, machine and rock matrix stiffnesses have been taken into

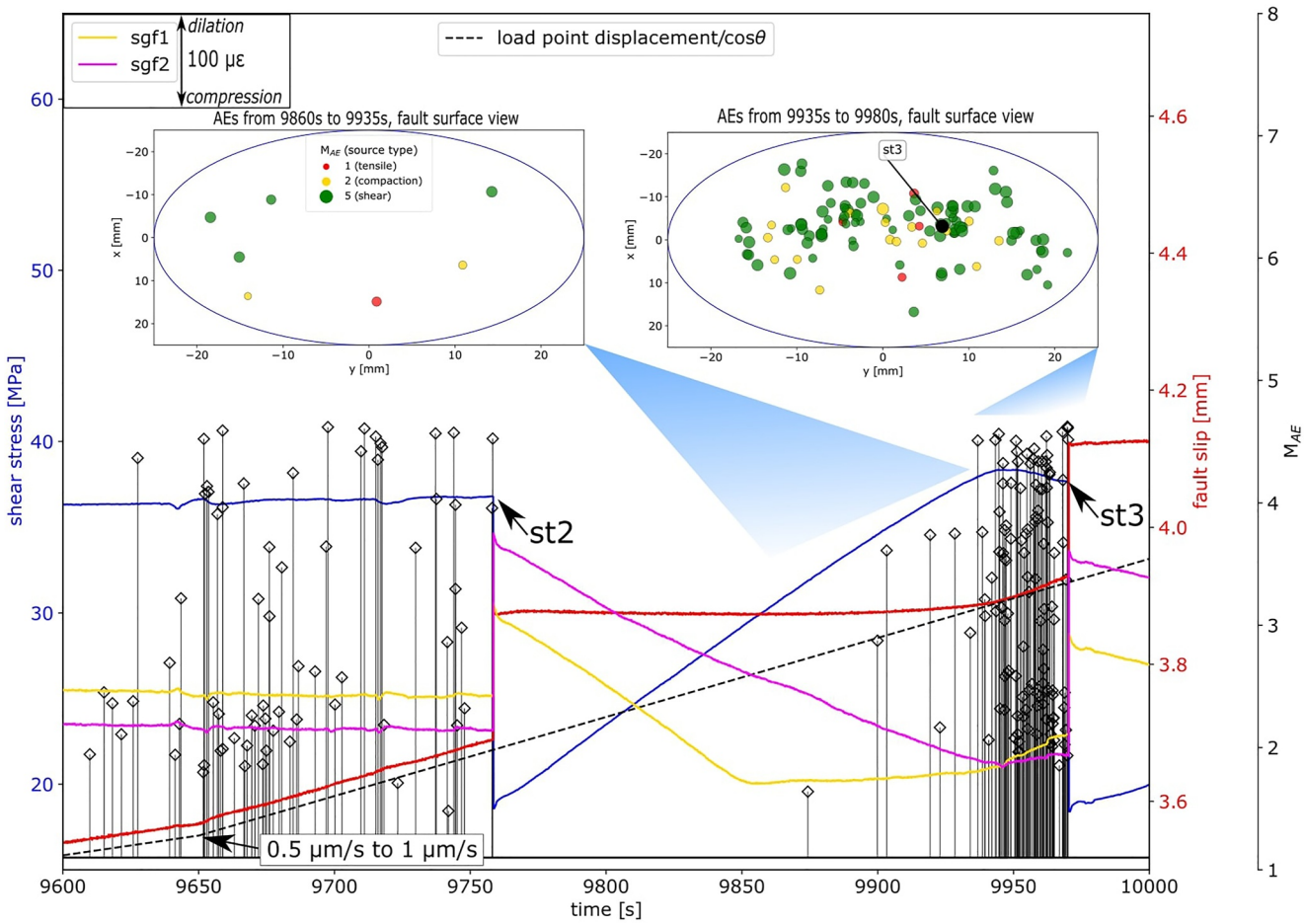

Figure 6. Rough fault evolution of shear stress, slip, AEs and strain signals prior to stick-slip events st2 and st3 for sample R1. Dashed black line gives load point displacement. Load point velocity was manually increased from 0.5 to 1 μm/s at $t = 9{,}650$ s. We indicate the locations of AEs occurring in the time window between $t = 9{,}860$ s and $t = 9{,}935$ s during which local slip occurred close to strain gage sgf1 (compare sgf1 (yellow) and sgf2 (pink) that remains in fault parallel shortening). (c) AE locations between $t = 9{,}935$ s to $t = 9{,}980$ s, corresponding to onset and acceleration of fault slip and beginning of fault parallel extension at sgf2 until the emergence of stick-slip event st3.

account in order to calculate the slip using Equation 5. The axial stiffness of loading system K_{system} is estimated as $K_{system} = 1/(1/K_{sample} + 1/K_{machine}) = 229$ MPa/mm, where $K_{sample} = E/L = 750$ MPa/mm is the elastic stiffness of the sample with E and L being Young's modulus and sample length, respectively. $K_{machine} = 330$ MPa/mm is the axial stiffness of loading machine.

To compare fault and loading system stiffness, we project fault slip and shear stress along the cylinder axis (z-axis) and loading direction. The resulting correction factor c (i.e., $c = 1/(\sin\theta \times \cos^2\theta) = 2.66$, see Equations 4 and 5) is used to estimate the equivalent axial stiffness of the fault. This results in the equivalent axial stiffness of the faults between 226 and 252 MPa/mm, which is comparable to axial stiffness of loading system K_{system}.

A summary of the mechanical data measured during the preparatory and coseismic phases during stick-slips is presented in Table 1.

4. Discussion

The results of this study provide new insights into the preparatory phase of seismic ruptures and the factors controlling frictional instabilities at the laboratory scale. In this section, we discuss how instabilities develop and how shear stress, slip and AE activity evolve during a stick-slip cycle. We compare our results to other studies

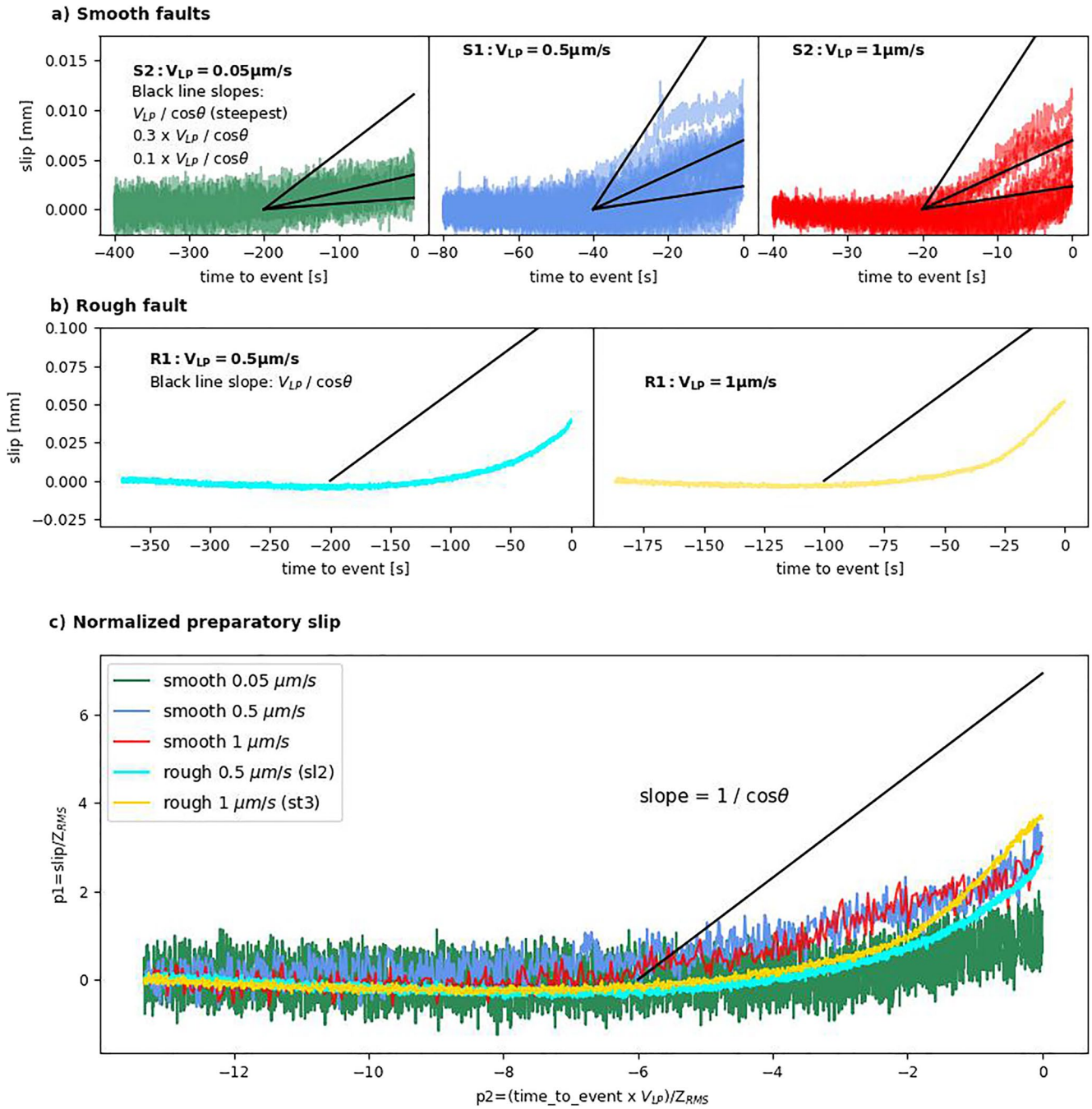

Figure 7. (a) Preparatory slip on smooth faults S1 and S2 prior stick-slips. The slopes of the solid black lines indicate the load point velocity projected on the fault plane v_{lp}/cosθ, as well as 0.3 v_{lp}/cosθ and 0.1 v_{lp}/cosθ. (b) Preparatory slip on the rough fault R1. (c) Dimensionless plot of slip normalized by roughness versus the time to events (instability) normalized by load point velocity and roughness (Z_{rms}). The slope corresponding to the load point displacement projected on the fault plane is also indicated by the solid black line and is equal to 1/cosθ in the dimensionless graph.

and discuss the observed stick-slip behavior based on estimates of fault stiffness and nucleation length. Then we discuss the role of fault roughness, load point velocity and fault surface evolution with progressive slip. Finally, we suggest a schematic model explaining the different effects of load point velocity on slip behavior of smooth versus rough faults.

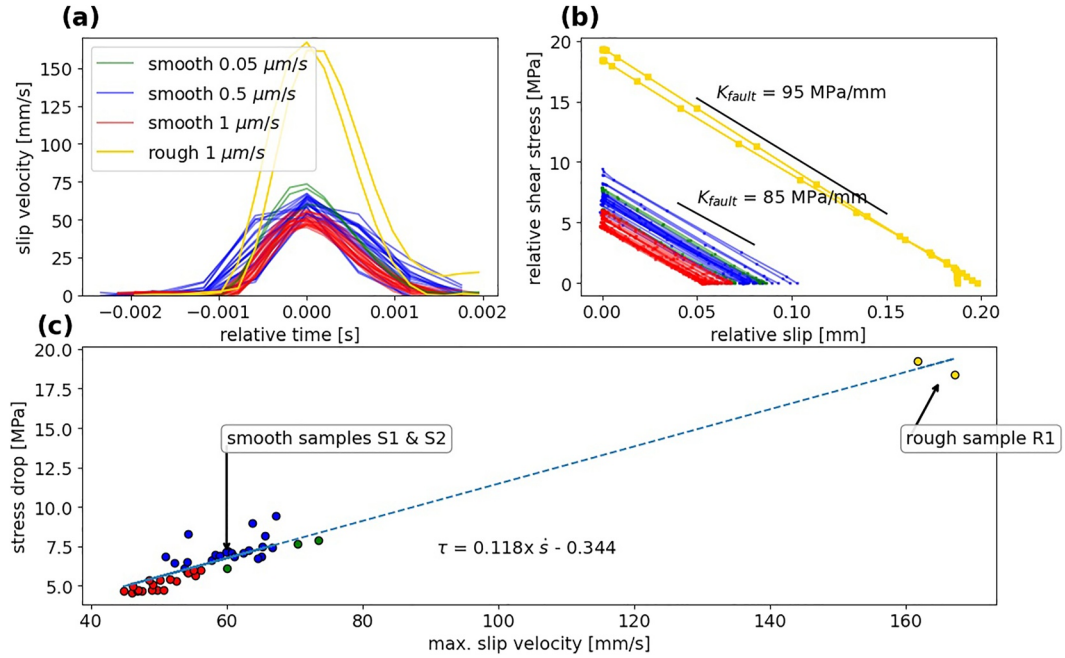

Figure 8. (a) Average slip velocity between the fault blocks recorded during stick-slip events on smooth faults at v_{lp} = 0.05 μm/s, 0.5 μm/s and 1 μm/s, and the rough fault at v_{lp} = 1 μm/s. (b) Shear stress versus fault slip during stick-slip events for the smooth faults and the rough fault. The slopes corresponding to fault stiffness are indicated with solid black lines. (c) Stress drop versus maximum slip velocities during stick-slip events on smooth and rough faults.

4.1. Stages of the Stick-Slip Cycle

From the combined mechanical data and AE characteristics of the experiments, a complex slip pattern emerges. Irrespective of roughness and load point velocity, we separate different general stages of the stick-slip cycle (Figure 9).

All faults are locked initially and samples deform elastically until fault slip starts (Stage 1 in Figure 9). Preparatory slip is 30–50 μm for rough faults but only 3–10 μm for smooth faults, before a stick-slip event occurs (Stages 2 and 3 in Figure 9). In rough faults, the distributed AEs at stage 2 indicate the presence of contacting asperities across the entire slipping fault which change in time and space. We note that for about 120s before event st3, a few AEs populate the periphery of the slip surface. This may indicate that slip starts preferentially from the outside of

Table 1
Summary of Measured Parameters During Preparatory and Coseismic Phases of Stick-Slips at Different Load Point Velocities for the Rough and Smooth Faults

	Smooth faults (Zrms = 3 μm)			Rough faults (Zrms = 14 μm)	
			Preparatory phase		
Load point velocity v_{lp} (μm/s)	0.05	0.5	1	0.5	1
Amount of preparatory slip (μm)	3	10	10	50	50
Duration of preparatory phase (s)	200	40	20	200	100
Preparatory slip velocity (percentage of v_{lp})		10 to 30		0 to ≥ 100	
			Coseismic phase		
Approximate fault stiffness (MPa/mm)			90		
Approximate coseismic slip duration (ms)			2		
Coseismic slip velocity (mm/s)	70	50 to 60	45 to 55	no high-speed data	160
Coseismic slip amount (μm)	80 to 85	70 to 100	50 to 70	175	200
Stress drop (MPa)	8	6 to 9	4.5 to 6	15.5	18 to 19

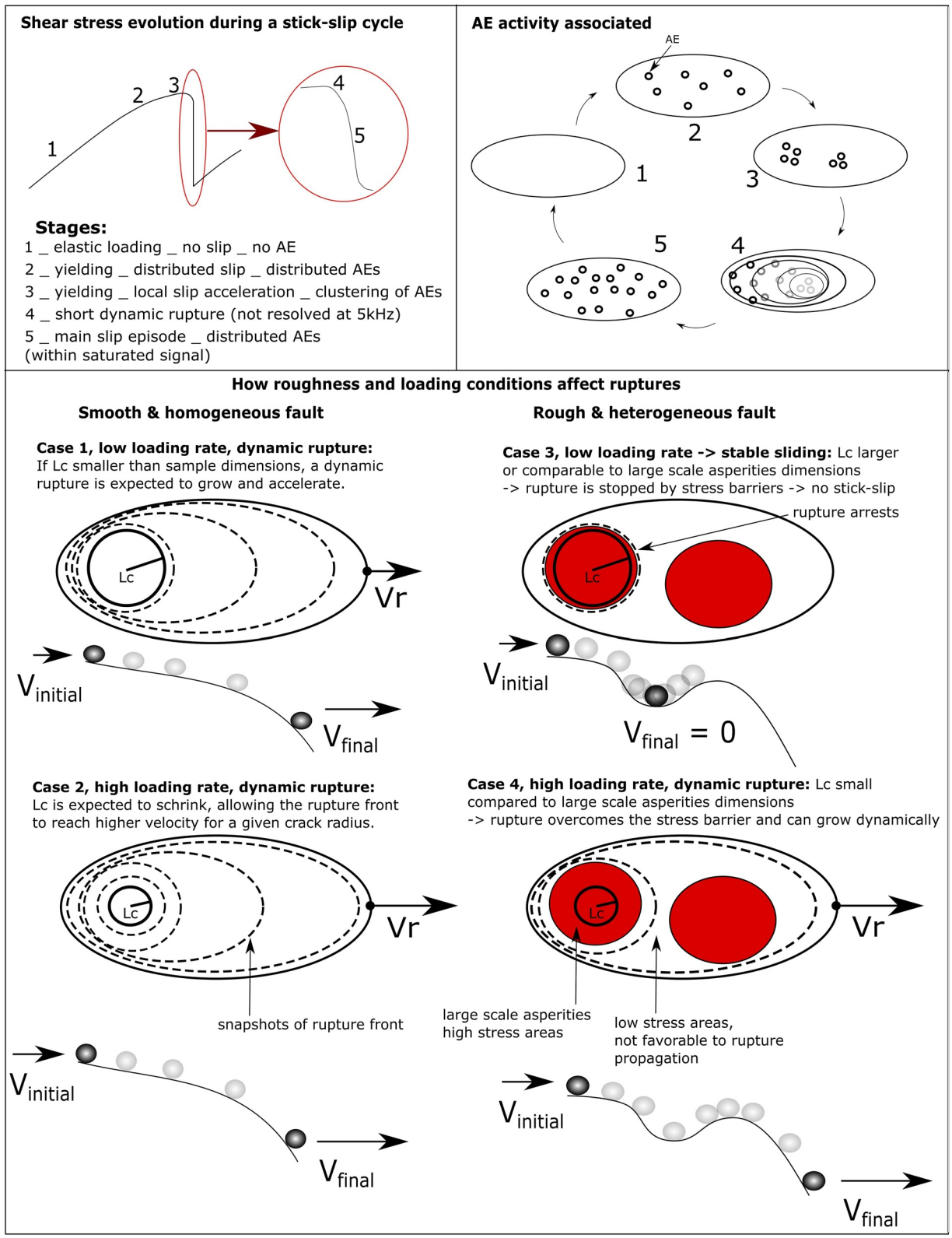

Figure 9. Interpretation of the rough fault behavior from mechanical and AE data. Stages 1–5 represent the different phases occurring during stick-slip experiments. Case 3 corresponds to a situation where no stick-slip would occur, but only a partial rupture/slow-slip event, while cases 1, 2, and 4 would lead to a dynamic rupture, and the stick-slip cycle would continue. We illustrate our idea with the analogy of a marble with different input velocities rolling down a bumpy slope.

the fault before localizing near the high stress asperities toward the center of the fault. As observed by Yamashita et al. (2022) this may be due to end effects and loading conditions. It is also conceivable that local slip close to the surface edges may have caused dilation, as observed on strain signal sgf1 at stage 2, but not on sgf2.

Precursory slip accelerates approaching failure but only for the rough faults slip rate reaches load point velocity at failure (Figure 3, st2, st3, Figures 5, Figure 6). On rough faults, AEs cluster along initial topographic highs that persist over several stick slip cycle (Figure 4). Asperities of contacting block surfaces produce normal stress heterogeneity across the fault surface (e.g., Cattania & Segall, 2021), which affect local shear stress and slip nucleation. AE clusters are collocated with high stress areas indicating accelerated local slip (stage 3, Figure 9). This agrees with nucleation of slip events observed in high stress areas in Guerin-Marthe et al. (2019). Local stress release at high stress areas was also reported by Dresen et al. (2020) and McLaskey and Lockner (2014) (Figure 6).

At failure (stages 4 and 5 in Figure 9), dynamic slip initiates from single or multiple asperities as indicated by single large AEs for smooth faults (associated with a loud audible noise, see Supporting Information S1) and clustered AEs for rough faults (Figure 6). Stage 4 may be compared to the nucleation phase as observed in previous experiments on large fault blocks (Guerin-Marthe et al., 2019; McLaskey, 2019), and may start or be ignited by a small AE as in McLaskey and Lockner (2014). Propagation of a rupture front was not observed directly, but could be resolved on strain gage signals from similar sawcut experiments on smooth faults intersected by a 7 mm diameter pin serving as asperity that reduced slip velocities to between 0.15 and 1 mm/s (Figure S7 in Supporting Information S1). For the slip events on rough and smooth faults observed, slip velocities were >45 mm/s and rupture propagation was likely faster than the maximum rupture velocity of 125 m/s resolvable at 5 kHz sampling rate.

Dynamic slip events affected the entire fault surface (stage 5, Figure 9), as indicated by slip and stress data (Figure 8) with sawcut samples behaving as a spring-slider system. This is supported by almost constant duration time of all stick-slip events of about 2 ms, irrespective of load point velocity or fault roughness (Figure 8). For a spring-slider system, duration (rise) time is defined as the natural oscillation period (Rice & Tse, 1986) controlled by system mass and stiffness (Shimamoto et al., 1980). This implies a linear relation between slip rate (particle velocity) and stress drop (Johnson & Scholz, 1976) of the spring-slider system in agreement with our observations (Figure 8c). We posit that for fast stick-slip events in all tests, passage of a dynamic rupture front results in a force imbalance as asperity contacts progressively detach (stage 4, Figure 9). Large amplitude acoustic events associated with fast stick slips produce long duration waveforms causing saturation of the recording system and enhanced noise level immediately following a slip event, masking small AEs for a time period right after slip onset. Following slip events, we always observed re-locking of the fault and elastic reloading without any AEs entering the next cycle with stage 1 (Figure 9; cf. Kwiatek, Charalampidou et al., 2014).

We commonly estimate nucleation length L_c of dynamic slip events and compare it with the sample's dimensions. Uenishi and Rice (2003), assume a slip-weakening friction law and estimate L_c as:

$$L_c = 1.158\frac{G}{K_f} \tag{6}$$

where G is shear modulus and K_f is slip weakening rate (here equivalent to fault unloading stiffness).

Given an average value of $K_f = 90$ MPa/mm measured during stage 5, and $G = 30$ GPa for La Peyratte granite, Equation 6 gives $L_c = 39$ cm, which exceeds the sample size, suggesting that dynamic slip should not occur. We posit that the discrepancy between L_c estimated from Equation 6 and our experimental observations is related to heterogeneous nucleation (Schär et al., 2021), and potentially complex weakening (Ben-Zion & Dresen, 2022; Paglialunga et al., 2022).

We suggest that most of the slip lasting about 2 ms corresponds to macroscopic frictional sliding outlasting rupture propagation. As discussed in Paglialunga et al. (2022), the stress versus slip evolution resolved may represent a long-tail frictional process over a slip distance that is much larger than the critical slip-weakening distance D_c (by a factor 50 in Paglialunga et al., 2022) associated with rapid local stress drop at a rupture front controlling fault stability.

For comparison, a critical patch size for slip instability h^* can also be obtained in the rate-and-state framework using the formulation of Rice (1993):

$$h^* = G \cdot d_c/(b-a) \cdot \sigma_n \tag{7}$$

Here, we assume $\sigma_n = 54$ MPa (approximate normal stress value measured for the rough fault), and a typical value of $b-a = 0.004$, as in McLaskey and Yamashita (2017). In the latter study, the characteristic rate-and-state slip distance d_c (which can be an order of magnitude smaller than D_c, see Cocco & Bizzarri, 2002) was taken at 1 μm and the gouge layer was estimated to a few tens of micrometers thick. As it has been shown that d_c decreases with fault gouge thickness (Marone & Kilgore, 1993) and our smooth faults show a very fine layer of gouge of maximum a few micrometers thick, taking $d_c = 0.1$ μm would give a value of $h^* \approx 1.38$ cm, consistent with the unstable behavior observed.

4.2. Effect of Fault Roughness

A plethora of studies showed that roughness plays an important role in controlling fault stability (Harbord et al., 2017; Morad et al., 2022; Ohnaka, 2003; Ohnaka & Shen, 1999; Okubo & Dieterich, 1984; Scholz, 1988), and that it introduces a nonuniform spatial distribution of local stresses, governing the preparatory and nucleation processes (Tal et al., 2018). On self-affine fault profiles, theoretical models of nucleation and rupture processes suggest that roughness generates an additional resistance to slip (roughness drag), which grows linearly with slip and progressively promotes slip heterogeneity and rupture arrests (Dieterich & Smith, 2009; Fang and Dunham. 2013; Tal et al., 2018). In early laboratory studies, Okubo and Dieterich (1984) showed that the critical slip-weakening distance D_c over which the stress reaches its residual level increases with roughness, and Ohnaka (2003) proposed an empirical scaling of D_c with a characteristic wavelength λ_c of the prepared rock surfaces. This means that the critical patch size or nucleation length required for a rupture to reach instability and accelerate to a dynamic rupture is larger for rough faults, assuming a constant stress drop. It has been confirmed by the laboratory experiments of Ohnaka and Shen (1999) and Xu et al. (2023). In agreement with this, we found that the amount of preparatory slip before slip events is larger on rough surfaces compared to smooth ones (Figure 5, Figures 7a and 7b), and that it scales with Z_{rms} (Figure 7c). Also, rough fault R1 was stable at a load point velocity of 0.5 μm/s and confining pressure of 35 MPa, while the smooth fault S1 is unstable at similar conditions. Note however that decreasing roughness does not always promote instability, as very smooth faults ($Z_{rms} < 1$ μm) were found to also exhibit stable behavior (Morad et al., 2022). Harbord et al. (2017) suggested that for smooth surfaces under high normal stress, the bridging length between contacts might become so small that instabilities cannot nucleate. In our tests, maximum slip rates and stress drops are larger for rough faults compared to smooth faults (Figure 8). This is in contrast to observation by Dresen et al. (2020) from tests performed on rough and smooth faults at significantly higher confining pressures of 130–150 MPa. However, in both studies larger stress drops occurred at higher stresses reached at the onset of slip, in agreement with findings of Passelegue et al. (2020).

Roughness clearly affects AE activity during preparatory slip (Dresen et al., 2020; Goebel et al., 2017). At similar monitoring conditions only few events were observed on smooth faults and preparatory slip was dominantly aseismic. In contrast, rough faults show strong AE activity, once fault slip commenced. AE source types reveal dominantly double-couple shear and compaction events. We posit that local concentration of shear and normal stresses related to the rough topography produce ubiquitous high frequency AEs leading to sample-wide slip events. In contrast, minor gouge production along smooth faults changes initial roughness Z_{rms} only slightly from about 3 to 5–6 μm compared to rough surfaces, where Z_{rms} of 12–16 μm remains unchanged. This suggests that smooth surfaces have larger contact areas with less pronounced stress concentration generating fewer AEs.

4.3. Effect of Load Point Velocity

Total preparatory slip was larger for rough compared to smooth faults but was not significantly affected by load point velocity. But as expected, increasing load point velocity reduced time to failure (Li & Rice, 1983). Increasing v_{lp} on rough faults (from 0.5 to 1 μm/s) also promoted instability (indicated by a large stress drop and slip amount during a short coseismic time window of approximately 2 ms), as previously observed at low fault normal stresses (Guérin-Marthe et al., 2019; Kato et al., 1992; McLaskey & Yamashita, 2017). These studies showed that increasing the load point velocity reduced the critical nucleation length L_c required for a dynamic rupture. Non-linear stability analysis of a spring-slider model including inertia effects suggested that the critical stiffness k_c increases with load point velocity (Gu et al., 1984). Using a continuum model and rate-and-state framework, Rubin and Ampuero (2005) showed that L_c decreased with increasing slip velocity V but was also affected by the state variable θ. A decrease of nucleation length with increasing load point velocity promotes dynamic failure of asperities with dimensions comparable to L_c.

In contrast, stick slip failure of smooth faults was less affected by changing v_{lp}. Increasing the load point velocity by a factor 20, from 0.05 to 1 μm/s reduced stress drop $\Delta\tau$ of stick-slip events from 7 to 5 MPa, and average slip rates decreased from 70–75 mm/s to 45–55 mm/s. Although the reason for the observed lower stress drops with increasing loading rate on sample S2 is not clear, it has also been observed in some other studies (Ohnaka, 1973). In the latter study, the sensitivity of the stress drop with load point velocity was influenced by the machine stiffness and the normal load. We posit that gouge production may also have affected stress drop in our experiments, as discussed below.

4.4. Effects of Cumulative Slip and Initial State of the Surface

Cumulative slip increases throughout experiments up to 4 mm on rough and 2.5 mm on smooth fault. Irrespective of wear and gouge production during slip, fault surface topography Z_{rms} is not affected very significantly by total slip as revealed by surface scans of samples S1, S2 and R1 before and after the tests (Figures S3 and S4 in Supporting Information S1). As shown on the scans of the postmortem surfaces for smooth fault S2, we found only a small amount of gouge covering mostly the center of the sawcut surfaces. Surface roughness Z_{rms} increased from 3 to 5–6 μm. The small amount of gouge production and changes in Z_{rms} had no significant effect on the mechanical behavior of the smooth faults (Figure 1a) except for a small hardening. If fault roughness increases with cumulative slip, L_c is expected to increase as well (Ohnaka, 2003). This would suggest that cumulative slip stabilizes fault slip, and that the change in load point velocity has a negligible effect in comparison. For rough faults, Z_{rms} and large asperities remained unchanged irrespective of gouge production. The power density spectra of the surfaces do not change significantly (Figure S5 in Supporting Information S1). This suggests that large-scale asperities (long-wavelength topography) do not evolve much with cumulative slip, in agreement with Goebel et al. (2017). Our observation clearly indicates that the mechanical response of the rough fault R1 is affected by changes in load point velocity rather than changes in surface topography with slip. For example, prior to slip event st2 the fault is stable at 0.05 μm/s, then becomes unstable at 1 μm/s, and stable again at 0.05 μm/s, despite the increase of cumulative slip in between. Note that although the observation of unstable behavior promoted at higher load point velocity on the rough fault is reproducible (see sample R2, Figure S8 and Text S2 in Supporting Information S1), small modification of the initial state of a surface (if we reuse a sample that underwent previous stick-slips with gouge remaining) may lead to a more pronounced surface evolution and to a different mechanical behavior at similar loading conditions.

4.5. Slip Behavior of Rough and Smooth Faults Loaded at Different Rates

AE hypocenters cluster on large asperities present on the rough sandblasted surfaces. If L_c is close to the asperity dimension, a rupture may start but will arrest if energy release at the rupture tip is insufficient to break or bypass neighboring barriers (Case 3, Figure 9) and potentially coalesce with other high stressed areas close to failure (Latour et al., 2013) (Case 4, Figure 9). For a rupture to break the entire sample surface, the local L_c needs to be small enough so that the rupture front breaks the large-scale asperity with enough energy remaining to keep propagating through stress or fracture energy barriers. This is similar to the condition needed to overcome stepovers as described in Lozos et al. (2014), and could be compared to the case of a marble rolling down a bumpy slope (Figure 9), with various initial energies. A decrease of L_c may occur when the load point velocity is increased. This would explain the two stick-slips st2 and st3 occurring in sample R1 at $v_{lp} = 1$ μm/s. Potentially, a small change of available energy at the rupture tip or a small change in load point velocity may decide whether or not a barrier is overcome, and if a dynamic rupture will occur.

On smooth faults, the mechanical behavior is different. First, almost no AEs were detected during the preparatory phase, from the onset of yielding until stick-slip. This may be due to small elevation of contacts which either creep or upon breaking do not necessarily trigger AEs above the noise level (cf. Kwiatek, Goebel, et al. (2014)). It is also consistent with the fact that smooth faults often produce less but larger AEs (Dresen et al., 2020; Goebel et al., 2017). Smooth faults are always unstable with regular stick-slip events for the whole range of load point velocities (0.05–1 μm/s). This is expected as L_c is smaller on smooth faults. Stress conditions of the smooth fault also favor dynamic rupture as the stresses are more homogeneous across the fault and low-stress barriers are absent. Surface roughness does not have a large characteristic wavelength locally controlling nucleation, rather a homogenized nucleation length L_c may be determined for the whole surface, and the effect of heterogeneities at a scale much lower than L_c may be averaged (Lebihain et al., 2021). For the smooth homogeneous fault, if L_c is

larger due to a lower load point velocity (Case 1 in Figure 9), the rupture may not accelerate as much, and reach slightly lower velocities. However, at homogeneous stress conditions, once the rupture is larger than the nucleation length, it will always accelerate and slip will become unstable in the absence of barrier. This would render small changes in load point velocity less important compared to heterogeneous rough faults.

4.6. Implications for Natural Earthquakes

We observed that a small increase in load point velocity by a factor of two promoted large stick-slip events on a heterogeneous rough fault. This suggests that in a natural setting locally enhanced loading rates may result in a transition from aseismic to seismic deformation, as discussed previously (e.g., Guerin-Marthe et al., 2019; McLaskey & Yamashita, 2017). This also suggests that small, local and transient perturbations during loading may result in large ruptures in a critically stressed fault zone (e.g., Kato & Ben-Zion, 2021). It has been suggested for ruptures on relatively smooth and mature faults that they were ignited by small local events (see McLaskey & Lockner, 2014), irrespective of the nucleation length for the entire fault. This sensitivity of earthquake nucleation to initial local conditions in nature renders interpretation of precursory signals even more difficult. As shown here for the controlled conditions of laboratory experiments, small changes in boundary conditions may result in a switch from regular series of stick-slip events to complex fault slip behavior with sudden stick-slip events occurring without noticeable precursory signals such as increase in AE activity (which could be regarded as foreshocks in nature). While the approximate recurrence time and stress drop of earthquakes on some large faults may be estimated (e.g., Shimazaki & Nakata, 1980), the nucleation of large earthquakes may result from small-scale stress fluctuations, making short-term prediction a big challenge.

5. Conclusions

In this study we compared the frictional behavior of a rough sandblasted fault (Zrms = 14 μm) and smooth faults (Zrms = 3 μm). We showed that:

- Increasing the load point velocity on the rough fault under triaxial conditions and at a confining pressure of 35 MPa promotes instability, as observed in previous studies at lower normal stress conditions.
- The amount of preparatory slip prior to stick-slip instabilities increases with fault roughness.
- The nucleation length derived using a slip-weakening law and an energy criterion, using the macroscopic averaged stress and slip along our fault surfaces does not explain the strong stick-slip instabilities observed, suggesting that local rupture processes are controlling the fault stability before any macroscopic frictional process can occur.
- AEs localize prior to rupture consistent with previous studies showing that the nucleation zone is preferentially located in high stressed areas.
- Inhomogeneities on rough surfaces render the failure mode of the fault sensitive to changes in load point velocity, as opposed to smoother surfaces where rupture initiates and propagates under homogeneous roughness and stress conditions.

Conflict of Interest

The authors declare no conflicts of interest relevant to this study.

Acknowledgments
S.G-M and P.M.G. acknowledge funding from the Helmholtz Association in the frame of the Young Investigators Group VH-NG-1232 (SAIDAN). The authors would also like to thank Michael Naumann and Stefan Gehrmann for the technical help, and Laboratoire Colas Centre Ouest for providing the La Peyratte granite samples. Finally, we thank the two anonymous reviewers and the associate editor for helping to clarify and improve the paper. Open Access funding enabled and organized by Projekt DEAL.

Data Availability Statement

The data used in this manuscript are available online (https://doi.org/10.5281/zenodo.6411819).

References

Ben-Zion, Y., & Dresen, G. (2022). A synthesis of fracture, friction and damage processes in earthquake rupture zones. *Pure and Applied Geophysics*, *179*(12), 4323–4339. https://doi.org/10.1007/s00024-022-03168-9

Bouchon, M., Durand, V., Marsan, D., Karabulut, H., & Schmittbuhl, J. (2013). The long precursory phase of most large interplate earthquakes. *Nature Geoscience*, *6*(4), 299–302. https://doi.org/10.1038/ngeo1770

Byerlee, J. D. (1970). The mechanics of stick-slip. *Tectonophysics*, *9*(5), 475–486. https://doi.org/10.1016/0040-1951(70)90059-4

Cattania, C., & Segall, P. (2021). Precursory slow slip and foreshocks on rough faults. *Journal of Geophysical Research: Solid Earth*, *126*(4), e2020JB020430. https://doi.org/10.1029/2020jb020430

Cocco, M., & Bizzarri, A. (2002). On the slip-weakening behavior of rate-and state dependent constitutive laws. *Geophysical Research Letters*, *29*(11), 11-1–11-4. https://doi.org/10.1029/2001GL013999

David, C., Menéndez, B., & Darot, M. (1999). Influence of stress-induced and thermal cracking on physical properties and microstructure of La Peyratte granite. *International Journal of Rock Mechanics and Mining Sciences*, *36*(4), 433–448. https://doi.org/10.1016/S0148-9062(99)00010-8

Dieterich, J. H., & Smith, D. E. (2009). Nonplanar faults: Mechanics of slip and off-fault damage. In *Mechanics, structure and evolution of fault zones* (pp. 1799–1815).

Dresen, G., Kwiatek, G., Goebel, T., & Ben-Zion, Y. (2020). Seismic and aseismic preparatory processes before large stick–slip failure. *Pure and Applied Geophysics*, *177*(12), 5741–5760. https://doi.org/10.1007/s00024-020-02605-x

Durand, V., Bentz, S., Kwiatek, G., Dresen, G., Wollin, C., Heidbach, O., et al. (2020). A two-scale preparation phase preceded an Mw 5.8 earthquake in the Sea of Marmara Offshore Istanbul, Turkey. *Seismological Research Letters*, *91*(6), 3139–3147. https://doi.org/10.1785/0220200110

Ellsworth, W. L., & Beroza, G. C. (1995). Seismic evidence for an earthquake nucleation phase. *Science*, *268*(5212), 851–855. https://doi.org/10.1126/science.268.5212.851

Fang, Z., & Dunham, E. M. (2013). Additional shear resistance from fault roughness and stress levels on geometrically complex faults. *Journal of Geophysical Research: Solid Earth*, *118*(7), 3642–3654. https://doi.org/10.1002/jgrb.50262

Font, Y., Kao, H., Lallemand, S., Liu, C. S., & Chiao, L. Y. (2004). Hypocentre determination offshore of eastern Taiwan using the maximum intersection method. *Geophysical Journal International*, *158*(2), 655–675. https://doi.org/10.1111/j.1365-246X.2004.02317.x

Goebel, T. H., Kwiatek, G., Becker, T. W., Brodsky, E. E., & Dresen, G. (2017). What allows seismic events to grow big?: Insights from b-value and fault roughness analysis in laboratory stick-slip experiments. *Geology*, *45*(9), 815–818. https://doi.org/10.1130/g39147.1

Goebel, T. H. W., Becker, T. W., Schorlemmer, D., Stanchits, S., Sammis, C., Rybacki, E., & Dresen, G. (2012). Identifying fault heterogeneity through mapping spatial anomalies in acoustic emission statistics. *Journal of Geophysical Research*, *117*(3), B03310. https://doi.org/10.1029/2011JB008763

Gu, J. C., Rice, J. R., Ruina, A. L., & Simon, T. T. (1984). Slip motion and stability of a single degree of freedom elastic system with rate and state dependent friction. *Journal of the Mechanics and Physics of Solids*, *32*(3), 167–196. https://doi.org/10.1016/0022-5096(84)90007-3

Guerin-Marthe, S. (2019). Analogue and numerical models of earthquake rupture, Chapter 5, 218. Retrieved from http://etheses.dur.ac.uk/13341/

Guérin-Marthe, S., Nielsen, S., Bird, R., Giani, S., & di Toro, G. (2019). Earthquake nucleation size: Evidence of loading rate dependence in laboratory faults. *Journal of Geophysical Research: Solid Earth*, *124*(1), 689–708. https://doi.org/10.1029/2018JB016803

Guo, Z., & Ogata, Y. (1997). Statistical relations between the parameters of aftershocks in time, space, and magnitude. *Journal of Geophysical Research*, *102*(B2), 2857–2873. https://doi.org/10.1029/96jb02946

Harbord, C. W. A., Nielsen, S. B., de Paola, N., & Holdsworth, R. E. (2017). Earthquake nucleation on rough faults. *Geology*, *45*(10), 931–934. https://doi.org/10.1130/G39181.1

Johnson, T. L., & Scholz, C. H. (1976). Dynamic properties of stick-slip friction of rock. *Journal of Geophysical Research*, *81*(5), 881–888. https://doi.org/10.1029/jb081i005p00881

Karner, S. L., & Marone, C. (2000). Effects of loading rate and normal stress on stress drop and stick-slip recurrence interval. In *Geophysical monograph series* (Vol. 120). https://doi.org/10.1029/GM120p0187

Kato, A., & Ben-Zion, Y. (2021). The generation of large earthquakes. *Nature Reviews Earth & Environment*, *2*(1), 26–39. https://doi.org/10.1038/s43017-020-00108-w

Kato, A., Obara, K., Igarashi, T., Tsuruoka, H., Nakagawa, S., & Hirata, N. (2012). Propagation of slow slip leading up to the 2011 Mw 9.0 Tohoku-Oki earthquake. *Science*, *335*(6069), 705–708. https://doi.org/10.1126/science.1215141

Kato, N., Yamamoto, K., Yamamoto, H., Hirasawa, T., Aki, K., Ohnaka, M., et al. (1992). Strain-rate effect on frictional strength and the slip nucleation process.

Kwiatek, G., Charalampidou, E. M., Dresen, G., & Stanchits, S. (2014a). An improved method for seismic moment tensor inversion of acoustic emissions through assessment of sensor coupling and sensitivity to incidence angle. *International Journal of Rock Mechanics and Mining Sciences*, *65*, 153–161. https://doi.org/10.1016/j.ijrmms.2013.11.005

Kwiatek, G., Goebel, T. H. W., & Dresen, G. (2014b). Seismic moment tensor and b value variations over successive seismic cycles in laboratory stick-slip experiments. *Geophysical Research Letters*, *41*(16), 5838–5846. https://doi.org/10.1002/2014GL060159

Latour, S., Schubnel, A., Nielsen, S., Madariaga, R., & Vinciguerra, S. (2013). Characterization of nucleation during laboratory earthquakes. *Geophysical Research Letters*, *40*(19), 5064–5069. https://doi.org/10.1002/grl.50974

Lebihain, M., Roch, T., Violay, M., & Molinari, J. F. (2021). Earthquake nucleation along faults with heterogeneous weakening rate. *Geophysical Research Letters*, *48*(21), e2021GL094901. https://doi.org/10.1029/2021gl094901

Li, V. C., & Rice, J. R. (1983). Precursory surface deformation in great plate boundary earthquake sequences. *Bulletin of the Seismological Society of America*, *73*(5), 1415–1434.

Lozos, J. C., Dieterich, J. H., & Oglesby, D. D. (2014). The effects of d0 on rupture Propagation on fault stepovers the effects of d0 on rupture propagation on fault stepovers. *Bulletin of the Seismological Society of America*, *104*(4), 1947–1953. https://doi.org/10.1785/0120130305

Marone, C. (1998). The effect of loading rate on static friction and the rate of fault healing during the earthquake cycle. *Nature*, *391*(6662), 69–72. https://doi.org/10.1038/34157

Marone, C., & Kilgore, B. (1993). Scaling of the critical slip distance for seismic faulting with shear strain in fault zones. *Nature*, *362*(6421), 618–621. https://doi.org/10.1038/362618a0

McLaskey, G. C. (2019). Earthquake initiation from laboratory observations and implications for foreshocks. *Journal of Geophysical Research: Solid Earth*, *124*(12), 12882–12904. https://doi.org/10.1029/2019JB018363

McLaskey, G. C., & Lockner, D. A. (2014). Preslip and cascade processes initiating laboratory stick slip. *Journal of Geophysical Research: Solid Earth*, *119*(8), 6323–6336. https://doi.org/10.1002/2014JB011220

Mclaskey, G. C., & Yamashita, F. (2017). Slow and fast ruptures on a laboratory fault controlled by loading characteristics. *Journal of Geophysical Research: Solid Earth*, *122*(5), 3719–3738. https://doi.org/10.1002/2016JB013681

Morad, D., Sagy, A., Tal, Y., & Hatzor, Y. H. (2022). Fault roughness controls sliding instability. *Earth and Planetary Science Letters*, *579*, 117365. https://doi.org/10.1016/j.epsl.2022.117365

Nelder, J. A., & Mead, R. (1965). A simplex method for function minimization. *The Computer Journal*, *7*(4), 308–313. https://doi.org/10.1093/comjnl/7.4.308

Ohnaka, M. (1973). Experimental studies of stick-slip and their application to the earthquake source mechanism. *Journal of Physics of the Earth*, *21*(3), 285–303. https://doi.org/10.4294/jpe1952.21.285

Ohnaka, M. (2003). A constitutive scaling law and a unified comprehension for frictional slip failure, shear fracture of intact rock, and earthquake rupture. *Journal of Geophysical Research*, *108*(B2), 2080. https://doi.org/10.1029/2000jb000123

Ohnaka, M., Kuwahara, Y., Yamamoto, K., & Hirasawa, T. (1986). Dynamic breakdown processes and the generating mechanism for high-frequency elastic radiation during stick-slip instabilities. *Earthquake Source Mechanics*, *37*, 13–24.
Ohnaka, M., & Shen, L. F. (1999). Scaling of the shear rupture process from nucleation to dynamic propagation: Implications of geometric irregularity of the rupturing surfaces. *Journal of Geophysical Research*, *104*(B1), 817–844. https://doi.org/10.1029/1998jb900007
Okubo, P. G., & Dieterich, J. H. (1984). Effects of physical fault properties on frictional instabilities produced on simulated faults. *Journal of Geophysical Research*, *89*(B7), 5817–5827. https://doi.org/10.1029/JB089iB07p05817
Paglialunga, F., Passelègue, F. X., Brantut, N., Barras, F., Lebihain, M., & Violay, M. (2022). On the scale dependence in the dynamics of frictional rupture: Constant fracture energy versus size-dependent breakdown work. *Earth and Planetary Science Letters*, *584*, 117442. https://doi.org/10.1016/j.epsl.2022.117442
Passelègue, F. X., Almakari, M., Dublanchet, P., Barras, F., Fortin, J., & Violay, M. (2020). Initial effective stress controls the nature of earthquakes. *Nature Communications*, *11*(1), 5132. https://doi.org/10.1038/s41467-020-18937-0
Rice, J. R. (1983). Constitutive relations for fault slip and earthquake instabilities. *Pure and Applied Geophysics PAGEOPH*, *121*(3), 443–475. https://doi.org/10.1007/BF02590151
Rice, J. R. (1993). Spatio-temporal complexity of slip on a fault. *Journal of Geophysical Research*, *98*(B6), 9885–9907. https://doi.org/10.1029/93jb00191
Rice, J. R., & Tse, S. T. (1986). Dynamic motion of a single degree of freedom system following a rate and state dependent friction law. *Journal of Geophysical Research*, *91*(B1), 521–530. https://doi.org/10.1016/0148-9062(86)90803-x
Ross, Z. E., Meier, M. A., & Hauksson, E. (2018). P wave arrival picking and first-motion polarity determination with deep learning. *Journal of Geophysical Research: Solid Earth*, *123*(6), 5120–5129. https://doi.org/10.1029/2017JB015251
Rubin, A. M., & Ampuero, J. P. (2005). Earthquake nucleation on (aging) rate and state faults. *Journal of Geophysical Research*, *110*(B11), B11312. https://doi.org/10.1029/2005jb003686
Ruina, A. (1983). Slip instability and state variable friction laws. *Journal of Geophysical Research*, *88*(B12), 10359–10370. https://doi.org/10.1029/jb088ib12p10359
Ruiz, S., Metois, M., Fuenzalida, A., Ruiz, J., Leyton, F., Grandin, R., et al. (2014). Intense foreshocks and a slow slip event preceded the 2014 Iquique Mw8.1 earthquake. *Science*, *345*(6201), 1165–1169. https://doi.org/10.1126/science.1256074
Schär, S., Albertini, G., & Kammer, D. S. (2021). Nucleation of frictional sliding by coalescence of microslip. *International Journal of Solids and Structures*, *225*, 111059. https://doi.org/10.1016/j.ijsolstr.2021.111059
Scholz, C., Molnar, P., & Johnson, T. (1972). Detailed studies of frictional sliding of granite and implications for the earthquake mechanism. *Journal of Geophysical Research*, *77*(32), 6392–6406. https://doi.org/10.1029/jb077i032p06392
Scholz, C. H. (1988). The critical slip distance for seismic faulting. *Nature*, *336*(6201), 761–763. https://doi.org/10.1038/336761a0
Shi, Y., & Bolt, B. A. (1982). The standard error of the magnitude-frequency b value. *Bulletin of the Seismological Society of America*, *72*(5), 1677–1687. https://doi.org/10.1785/bssa0720051677
Shimamoto, T., Handin, J., & Logan, J. M. (1980). Specimen-apparatus interaction during stick-slip in a tri axial compression machine: A decoupled two-degree-of-freedom model. *Tectonophysics*, *67*(3–4), 175–205. https://doi.org/10.1016/0040-1951(80)90234-6
Shimazaki, K., & Nakata, T. (1980). Time-predictable recurrence model for large earthquakes. *Geophysical Research Letters*, *7*(4), 279–282. https://doi.org/10.1029/gl007i004p00279
Stanchits, S., Mayr, S., Shapiro, S., & Dresen, G. (2011). Fracturing of porous rock induced by fluid injection. *Tectonophysics*, *503*(1–2), 129–145. https://doi.org/10.1016/j.tecto.2010.09.022
Tal, Y., Hager, B. H., & Ampuero, J. P. (2018). The effects of fault roughness on the earthquake nucleation process. *Journal of Geophysical Research: Solid Earth*, *123*(1), 437–456. https://doi.org/10.1002/2017jb014746
Tape, C., Holtkamp, S., Silwal, V., Hawthorne, J., Kaneko, Y., Ampuero, J. P., et al. (2018). Earthquake nucleation and fault slip complexity in the lower crust of central Alaska. *Nature Geoscience*, *11*(7), 536–541. https://doi.org/10.1038/s41561-018-0144-2
Uenishi, K., & Rice, J. R. (2003). Universal nucleation length for slip-weakening rupture instability under nonuniform fault loading. *Journal of Geophysical Research*, *108*(B1), 2042. https://doi.org/10.1029/2001JB001681
Wang, L., Kwiatek, G., Rybacki, E., Bonnelye, A., Bohnhoff, M., & Dresen, G. (2020). Laboratory study on fluid-induced fault slip behavior: The role of fluid pressurization rate. *Geophysical Research Letters*, *47*(6), e2019GL086627. https://doi.org/10.1029/2019GL086627
Xu, S., Fukuyama, E., Yamashita, F., Kawakata, H., Mizoguchi, K., & Takizawa, S. (2023). Fault strength and rupture process controlled by fault surface topography. *Nature Geoscience*, *16*, 1–7. https://doi.org/10.1038/s41561-022-01093-z
Yamashita, F., Fukuyama, E., & Xu, S. (2022). Foreshock activity promoted by locally elevated loading rate on a 4-m-Long laboratory fault. *Journal of Geophysical Research: Solid Earth*, *127*(3), e2021JB023336. https://doi.org/10.1029/2021jb023336
Yamashita, F., Fukuyama, E., Xu, S., Kawakata, H., Mizoguchi, K., & Takizawa, S. (2021). Two end-member earthquake preparations illuminated by foreshock activity on a meter-scale laboratory fault. *Nature Communications*, *12*(1), 4302. https://doi.org/10.1038/s41467-021-24625-4
Zang, A., Wagner, F. C., Stanchits, S., Dresen, G., Andresen, R., & Haidekker, M. A. (1998). Source analysis of acoustic emissions in Aue granite cores under symmetric and asymmetric compressive loads. *Geophysical Journal International*, *135*(3), 1113–1130. https://doi.org/10.1046/j.1365-246X.1998.00706.x
Zhuo, Y.-Q., Liu, P., Guo, Y., Chen, H., Chen, S., & Wang, K. (2022). Cross-effects of loading rate and cumulative fault slip on pre-seismic rupture and unstable slip rate of laboratory earthquakes. *Tectonophysics*, *826*, 229266. https://doi.org/10.1016/j.tecto.2022.229266

References From the Supporting Information

Eshelby, J. D. (1957). The determination of the elastic field of an ellipsoidal inclusion, and related problems. *Proceedings of the Royal Society of London - Series A: Mathematical and Physical Sciences*, *241*(1226), 376–396.
Svetlizky, I., & Fineberg, J. (2014). Classical shear cracks drive the onset of dry frictional motion. *Nature*, *509*(7499), 205–208. https://doi.org/10.1038/nature13202